Lipid droplet-associated kinase STK25 regulates peroxisomal activity and metabolic stress response in steatotic liver[S]

Annika Nerstedt,* Yeshwant Kurhe,[1,*] Emmelie Cansby,[1,*] Mara Caputo,* Lei Gao,* Egor Vorontsov,[†] Marcus Ståhlman,[§] Esther Nuñez-Durán,* Jan Borén,[§] Hanns-Ulrich Marschall,[§] Douglas G. Mashek, Darren N. Saunders,[††] Carina Sihlbom,[†] Andrew J. Hoy,[§§] and Margit Mahlapuu[2,*]**

Departments of Chemistry and Molecular Biology* and Molecular and Clinical Medicine/Wallenberg Laboratory, Institute of Medicine,[§] University of Gothenburg and Sahlgrenska University Hospital, Gothenburg, Sweden; Proteomics Core Facility,[†] University of Gothenburg, Gothenburg, Sweden; Department of Biochemistry, Molecular Biology, and Biophysics,** University of Minnesota, Minneapolis, MN; School of Medical Sciences,[††] Faculty of Medicine, University of New South Wales, Sydney, NSW, Australia; and Discipline of Physiology,[§§] School of Medical Sciences, Charles Perkins Centre, University of Sydney, Sydney, NSW, Australia

ORCID IDs: 0000-0002-2607-6236 (A.N.); 0000-0001-5537-3427 (Y.K.); 0000-0003-1589-3596 (E.C.); 0000-0002-4202-0339 (M.S.); 0000-0003-0786-8091 (J.B.); 0000-0001-7347-3085 (H-U.M.); 0000-0001-7033-3386 (D.G.M.); 0000-0003-3922-1137 (A.J.H.); 0000-0001-8740-8874 (M.M.).

Abstract Nonalcoholic fatty liver disease (NAFLD) and nonalcoholic steatohepatitis (NASH) are emerging as leading causes of liver disease worldwide and have been recognized as one of the major unmet medical needs of the 21st century. Our recent translational studies in mouse models, human cell lines, and well-characterized patient cohorts have identified serine/threonine kinase (STK)25 as a protein that coats intrahepatocellular lipid droplets (LDs) and critically regulates liver lipid homeostasis and progression of NAFLD/NASH. Here, we studied the mechanism-of-action of STK25 in steatotic liver by relative quantification of the hepatic LD-associated phosphoproteome from high-fat diet-fed *Stk25* knockout mice compared with their wild-type littermates. We observed a total of 131 proteins and 60 phosphoproteins that were differentially represented in STK25-deficient livers. Most notably, a number of proteins involved in peroxisomal function, ubiquitination-mediated proteolysis, and antioxidant defense were coordinately regulated in *Stk25*$^{-/-}$ versus wild-type livers. We confirmed attenuated peroxisomal biogenesis and protection against oxidative and ER stress in STK25-deficient human liver cells, demonstrating the hepatocyte-autonomous manner of STK25's action. In summary, our results suggest that regulation of peroxisomal function and metabolic stress response may be important molecular mechanisms by which STK25 controls the development and progression of NAFLD/NASH.—Nerstedt, A., Y. Kurhe, E. Cansby, M. Caputo, L. Gao, E. Vorontsov, M. Ståhlman, E. Nuñez-Durán, J. Borén, H-U. Marschall, D. G. Mashek, D. N. Saunders, C. Sihlbom, A. J. Hoy, and M. Mahlapuu. **Lipid droplet-associated kinase STK25 regulates peroxisomal activity and metabolic stress response in steatotic liver. *J. Lipid Res.* 2020.** 61: **178–191.**

Supplementary key words protein kinases • nonalcoholic fatty liver disease • steatohepatitis • serine/threonine kinase 25

Nonalcoholic fatty liver disease (NAFLD), defined as fatty infiltration in >5% of hepatocytes (steatosis) in the absence of excessive alcohol consumption, is emerging as a leading cause of liver disease worldwide (1). Subjects with NAFLD have an increased risk of progressing into nonalcoholic

This work was supported by grants from the Swedish Research Council, the European Foundation for the Study of Diabetes/Novo Nordisk Programme for Diabetes Research in Europe, the West Sweden Avtal om Läkarutbildning och Forskning (ALF) Program, the Novo Nordisk Foundation, the Swedish Heart-Lung Foundation, the Torsten Söderbergs Foundation, the Swedish Diabetes Foundation, the Royal Society of Arts and Sciences in Gothenburg, the Åke Wiberg Foundation, the Adlerbert Research Foundation, the I. Hultman Foundation, the S. and E. Goljes Foundation, the F. Neubergh Foundation, the Prof. N. Svartz Foundation, the L. and J. Grönberg Foundation, the W. and M. Lundgren Foundation, and the I-B. and Å. Lundbergs Research Foundation. A.J.H. is supported by a University of Sydney Robinson Fellowship. The authors declare that they have no conflicts of interest with the contents of this article.

Manuscript received 6 August 2019 and in revised form 5 November 2019.

Published, JLR Papers in Press, December 19, 2019
DOI https://doi.org/10.1194/jlr.RA119000316

Abbreviations: ASO, antisense oligonucleotide; DHE, dihydroethidium; FABP1, fatty acid binding protein; GSTT, glutathione s-transferase theta; IHH, immortalized human hepatocyte; JNK, c-Jun-N-terminal kinase; LD, lipid droplet; NAFLD, nonalcoholic fatty liver disease; NASH, nonalcoholic steatohepatitis; NTC, nontargeting control; PTS1, peroxisomal targeting signal 1; SDS, sodium dodecyl sulfate; STK, serine/threonine kinase; TAG, triacylglycerol; TEAB, triethylammonium bicarbonate; TMT, tandem mass tag; VLCFA, very long chain fatty acid.

The MS proteomics data, including the annotated spectra, have been deposited to the ProteomeXchange Consortium via the PRIDE (79) partner repository with the dataset identifier PXD015311.

[1]Y. Kurhe and E. Cansby contributed equally to this work.

[2]To whom correspondence should be addressed.
e-mail: Margit.Mahlapuu@gu.se

[S] The online version of this article (available at https://www.jlr.org) contains a supplement.

steatohepatitis (NASH) as well as developing type 2 diabetes, cardiovascular disease, and liver cancer (2–4). Thus, understanding the pathobiology of NAFLD is of high medical relevance for the efficient prevention and treatment of a range of complex metabolic diseases.

In NAFLD, excess lipids accumulate within intrahepatocellular lipid droplets (LDs), which are composed of a neutral lipid core of mainly triacylglycerol (TAG) and cholesterol esters surrounded by a phospholipid monolayer that harbors specific proteins. Once thought to be only inert energy storage depots, hepatic LDs are increasingly recognized as organelles that not only orchestrate liver lipid partitioning but also play a critical role in protein quality control and storage, cell signaling, and viral replication (5). Notably, LDs dynamically interact with a variety of cellular organelles including the ER, mitochondria, peroxisomes, and endosomes (6). Liver LD surface-associated proteins regulate the functional properties of LDs, and the composition of hepatic LD proteins is dynamically influenced by dietary fat content as well as liver metabolic status (7, 8). Consequently, exploring how LD-coating proteins affect hepatic lipid homeostasis is important for understanding the molecular pathophysiology of NAFLD.

In the search for novel targets that regulate ectopic lipid accumulation in the context of nutritional stress and obesity, we identified serine/threonine kinase (STK)25, a member of the Ste20 kinase superfamily (9), as a hepatic LD-associated protein, which critically controls the development and progression of NAFLD (10–15). We found that STK25 knockdown attenuates lipid deposition in human hepatocytes and mouse liver by repressing lipid synthesis and enhancing β-oxidation and VLDL-TAG secretion, with the reciprocal phenotype seen when STK25 protein is overexpressed (10–14). Notably, administration of hepatocyte-targeting GalNAc-conjugated *Stk25* antisense oligonucleotide (ASO) in obese mice effectively ameliorates high-fat diet-induced hepatic steatosis as well as NASH features (i.e., liver inflammation, hepatocellular ballooning, and fibrosis), providing in vivo nonclinical proof-of-principle for the metabolic benefit of pharmacological STK25 inhibitors (15). Furthermore, we observed that STK25 mRNA and protein levels in human liver biopsies correlate with the severity of NASH, and several common nonlinked SNPs in the human *STK25* gene are associated with altered liver fat content (12–14). Although these studies suggest a key role for STK25 in the control of liver LD dynamics, the mechanism-of-action of STK25 in regulation of hepatic lipid partitioning has remained elusive.

To provide novel insights into the biological function of STK25 in the liver under steatotic conditions, we here characterized the hepatic LD-associated phosphoproteome in *Stk25* knockout mice and their wild-type littermates following high-fat diet feeding using a nonbiased approach by isobaric tagging for relative quantification. Of the 4,515 proteins and 982 phosphoproteins identified with a 1% false discovery rate, we report a total of 131 proteins and 60 phosphoproteins that were differentially represented in STK25-deficient livers. Most notably, a number of proteins involved in peroxisomal function, ubiquitination-mediated proteolysis, and antioxidant defense were coordinately regulated in the livers from high-fat diet-fed *Stk25*$^{-/-}$ mice compared with wild-type controls.

MATERIALS AND METHODS

Mice

Stk25 knockout mice were generated by deletion of exons 4 and 5 and genotyped as previously described (16). Heterozygous mice were backcrossed to a C57BL6/J genetic background, and the heterozygous mice were then intercrossed to obtain the homozygotes used in all experiments. From the age of 6 weeks, male knockout mice and their wild-type littermates were fed a pelleted high-fat diet (45% kilocalories from fat; D12451; Research Diets, New Brunswick, NJ) for 18 weeks. At the age of 24 weeks, the mice were euthanized after 4 h of food withdrawal and livers were collected for preparation of LDs. Histological evaluation performed in our previous study revealed that wild-type male mice fed an identical high-fat diet for 20 weeks developed pronounced macro- and microvesicular steatosis in the liver, whereas markedly less hepatic lipid accumulation was observed in high-fat-fed *Stk25*$^{-/-}$ mice (about 2-fold reduction in the total lipid area) (10). However, as whole livers were used for LD preparation in this study, it was not possible to perform histological or biochemical characterization of the extent of diet-induced liver damage in these mice. All animal experiments were performed after approval from the local Ethics Committee for Animal Studies at the Administrative Court of Appeals in Gothenburg, Sweden, and followed appropriate guidelines.

LC-MS analysis of mouse liver LDs

LC-MS analysis included five biological replicates per genotype and no technical replicates due to the small sample amount. The livers were minced, resuspended in 4 ml of buffer A [25 mmol/l tricene (Sigma-Aldrich, St. Louis, MO), 250 mmol/l sucrose (Sigma-Aldrich), and protease inhibitor cocktail (Thermo Fisher Scientific, Waltham, MA)] and dounce homogenized on ice, followed by further homogenization using a 25 gauge needle and a syringe. After addition of 4 ml of buffer A, the postnuclear supernatant was divided into two ultracentrifuge tubes, overlaid with 3 ml of buffer B [20 mmol/l HEPES, 100 mmol/l KCl, and 2 mmol/l $MgCl_2$ (Sigma-Aldrich)] and centrifuged at 300,000 *g* for 1 h at 4°C. The LD-containing band was transferred into a fresh tube and centrifuged at 20,000 *g* for 20 min at 4°C. The underlying liquid was carefully removed and the LD fraction was washed four times with buffer B to remove copurifying membranes (17, 18). The isolated LDs were then stored at –80°C until further analysis.

For LC-MS analysis, the liver LD preparations were mixed at 4°C with the Pierce phosphatase inhibitor ×2 solution (Invitrogen, Carlsbad, CA) and 16% sodium dodecyl sulfate (SDS)/200 mmol/l triethylammonium bicarbonate (TEAB) to a final concentration of approximately 1.5% SDS. The solution was centrifuged at 13,500 *g* for 20 min and the colorless protein extract layer was transferred to a separate vial. The remaining white top layer was then washed with 110 μl of the solution containing the phosphatase inhibitor at ×0.5 concentration, 1.5% SDS, and 20 mmol/l TEAB, and centrifuged at 13,500 *g* for 20 min; the colorless aqueous layer was collected and combined with the protein extract from the previous step. Protein concentrations in the combined protein extracts were determined using the Pierce BCA protein assay (Pierce Biotechnology, Rockford, IL) and the Benchmark Plus microplate reader (Bio-Rad, Hercules, CA). Aliquots containing 180 μg of protein were digested with trypsin using the filter-aided sample preparation method (19). In brief, the samples were incubated with 100 mmol/l dithiothreitol at 60°C for 30 min, transferred onto the 30 kDa MWCO Nanosep centrifugal filters (Pall Life Sciences, Ann Arbor, MI), washed with 8 M urea solution, and alkylated with 10 mmol/l methyl methanethiosulfonate in 50 mmol/l TEAB and 1% sodium deoxycholate. Digestion was

performed in 50 mmol/l TEAB/1% sodium deoxycholate at 37°C in two stages: the samples were incubated with 1.8 μg of Pierce MS-grade trypsin (trypsin to protein ratio 1:100; Pierce Biotechnology) overnight; then 1.8 μg of trypsin were added, and the digestion was performed for three additional hours. The peptides were collected by centrifugation and labeled using tandem mass tag (TMT) 10-plex isobaric mass tagging reagents (Pierce Biotechnology) according to the manufacturer's instructions. The labeled samples were mixed and sodium deoxycholate was removed by acidification with 10% trifluoroacetic acid and subsequent centrifugation at 13,500 *g*. An aliquot containing approximately 90 μg of the pooled labeled peptide mixture (1/20 of the total amount by volume) was fractionated using the Pierce high pH reversed-phase peptide fractionation kit (Pierce Biotechnology) according to the manufacturer's recommendations. Eight fractions were collected using the elution solvents containing 0.1% of triethylamine and 10.0, 12.0, 14.0, 16.0, 18.0, 20.0, 22.5, and 50.0% of acetonitrile. The fractions were dried on Speedvac and reconstituted in 3% acetonitrile/0.2% formic acid for analysis.

For the phosphopeptide enrichment, the remaining part (19/20 of the total volume) of the pooled TMT-labeled peptide sample (approximately 1,700 μg) was divided into two equal aliquots and both aliquots were evaporated on Speedvac to dryness. One aliquot was resuspended in the buffer and processed using the Pierce TiO_2 phosphopeptide enrichment and clean up kit (Pierce Biotechnology) according to the manufacturer's protocol. Another aliquot was resuspended in the buffer and processed using the High-Select Fe-NTA phosphopeptide enrichment kit (Thermo Fisher Scientific) according to the manufacturer's protocol. In both cases, the enriched samples were purified using the Pierce C18 spin columns (8 mg of the C18 material; Pierce Biotechnology), and the purified samples were then dried on Speedvac. TMT-labeled phosphopeptides from both TiO_2 and Fe-NTA enrichment were reconstituted in 3% acetonitrile/0.2% formic acid and analyzed separately.

All the samples were analyzed on an Orbitrap Fusion Tribrid mass spectrometer (Thermo Fisher Scientific) interfaced with an Easy-nLC 1200 nanoflow LC system (Thermo Fisher Scientific). Peptides were trapped on the Acclaim Pepmap 100 C18 trap column (100 μm × 2 cm, particle size 5 μm; Thermo Fisher Scientific) and separated on the in-house packed C18 analytical column (packing material 75 μm × 30 cm, particle size 3 μm; Dr. Maisch, Ammerbuch, Germany) using 0.2% formic acid as eluent A and 80% acetonitrile/0.2% formic acid as eluent B. For the whole proteome fractions, the gradient was from 5% to 33% B for 105 min, from 33% to 100% B for 5 min, and 100% B for 10 min. The above-mentioned gradient was also used for both phosphopeptide-enriched samples, and the TiO_2-enriched samples were additionally analyzed using the gradient from 3% to 25% B for 105 min, from 25% to 100% B for 5 min, and 100% B for 10 min. The precursor ion spectra were recorded at 120,000 resolution, the most intense precursor ions were selected ("top speed" setting with a duty cycle of 3 s), fragmented using collision-induced dissociation at collision energy setting of 35, and the MS2 spectra were recorded in ion trap with the maximum injection time of 50 ms and the isolation window of 0.7 Da. Charge states 2–7 were selected for fragmentation and dynamic exclusion was set to 45 s with 10 ppm tolerance. MS3 spectra for reporter ion quantitation were recorded at 50,000 resolution with higher-energy collisional dissociation fragmentation at collision energy of 60 using the synchronous precursor selection of the seven most abundant MS2 fragments, with the maximum injection time of 100 ms. In order to increase the depth of the phosphopeptide analysis, the Fe-NTA-enriched samples were additionally analyzed using the neutral loss-triggered TMT MS3 method with the neutral loss of phosphoric acid. Furthermore, the lists of the identified peptides for the first data-dependent acquisitions of both phosphopeptide samples were used to create the exclusion mass lists, and both samples were reanalyzed using the data-dependent TMT MS3 method that excluded the masses of the previously identified peptides from the data-dependent selection.

Data analysis was performed using Proteome Discoverer version 2.2 (Thermo Fisher Scientific). The database search was performed against the Swissprot *Mus musculus* database (October 2017), Mascot 2.5.1 (Matrix Science, London, UK) was used as a search engine with precursor mass tolerance of 10 ppm and fragment mass tolerance of 0.6 Da; tryptic peptides with one missed cleavage were accepted, mono-oxidation on methionine was set as a variable modification, methylthiolation on cysteine and TMT-6 reagent modification on lysine and peptide N terminus were set as a fixed modification for all files; phosphorylation on serine, threonine, and tyrosine was set as a variable modification for the processing of the phosphopeptide-enriched samples. Trypsin cleaves at the carboxylic side of lysine and arginine when the next amino acid is not proline. Percolator (Matrix Science) was used for the validation of identification results with the strict target false discovery rate of 1%. Reporter ion intensities were quantified in MS3 spectra at 0.003 Da mass tolerance and normalized on the total protein abundance within the Proteome Discoverer 2.2 (Thermo Fisher Scientific). Only the quantification values from the unique peptides were used for quantification. We estimated the uncertainty for correct peptide sequence to be 1%, as we filtered for false discovery rate 1% toward a decoy database, and the uncertainty in quantification to be less than 20% based on previous validation of this method. KEGG pathway analysis was performed using STRING (v10) (20) (with a confidence score of 0.700) and Cytoscape (v3.1.1) (21).

Immunofluorescence analysis of mouse liver sections

Liver samples were fixed with 4% (vol/vol) phosphate-buffered formaldehyde (Histolab Products, Gothenburg, Sweden), embedded in paraffin, and sectioned. Liver sections were incubated with primary antibodies, followed by incubation with fluorescent-dye-conjugated secondary antibodies (see supplemental Table S1 for antibody information). The PEX5-positive area was quantified in six randomly selected microscopic fields (×40) per mouse using the ImageJ software (1.47v; National Institutes of Health, Bethesda, MD).

Measurement of VLCFAs and plasmalogens in mouse liver lysates

Liver lipids were extracted using the BUME method and an aliquot of the total lipid extract was further treated with methanol and heptane to remove the neutral lipids (TAGs and cholesteryl esters) and purify the phospholipid fraction (22). From this fraction, the plasmalogens were analyzed using direct infusion MS as previously described (23, 24). For this a robotic nanoflow ion source, TriVersa NanoMate (Advion BioSciences, Ithaca, NJ) was used together with a QTRAP 5500 mass spectrometer (Sciex, Concord, Ontario, Canada). For analysis of very long chain fatty acids (VLCFAs), an aliquot of the phospholipid fraction was hydrolyzed by incubating at 50°C overnight in 300 μl of acetonitrile:concentrated HCl (4:1). After cooling to room temperature, the free fatty acids were extracted using 600 μl of iso-hexane. The hexane phase was evaporated and the fatty acids were reconstituted in 100 μl of chloroform:methanol (1:2) with 5 mmol/l ammonium acetate. Analysis and detection of the VLCFAs were made using direct infusion MS as previously reported (25).

Culture, RNA interference, and immunofluorescence analysis of immortalized human hepatocytes

Immortalized human hepatocytes [IHHs; a gift from B. Staels, Pasteur Institute of Lille, University of Lille Nord de France, Lille, France (26)] were maintained in William's E medium (GlutaMAX supplemented; Gibco, Paisley, UK) supplemented with human insulin (20 U/l; Actrapid Penfill; Novo Nordisk, Bagsværd, Denmark), dexamethasone (50 nmol/l; Sigma-Aldrich), 10% (vol/vol) FBS (Gibco), and 1% (vol/vol) penicillin/streptomycin (Gibco). Cells were demonstrated to be free of mycoplasma infection by use of the MycoAlert mycoplasma detection kit (Lonza, Basel, Switzerland). IHHs were transfected with *STK25* siRNA (s20570; Ambion, Austin, TX) or scrambled siRNA (SIC001; Sigma-Aldrich) using Lipofectamine RNAiMax (Invitrogen). Before the experiments, cells were exposed to 50 μmol/l oleic acid (Sigma-Aldrich) for 48 h in order to mimic conditions in high-risk individuals. In some experiments, cells were also treated with 1 μmol/l MG132 (474790; Calbiochem, San Diego, CA) for 24 h to inhibit proteasome function in hepatocytes (27, 28). Cells were processed for immunofluorescence with anti-PEX5, anti-catalase, anti-HNE, or anti-KDEL antibodies (see supplemental Table S1 for antibody information); the labeled area was quantified in six randomly selected microscopic fields (×20) per well using the ImageJ software (1.47v; National Institutes of Health). For dihydroethidium (DHE) staining, cells were incubated with 5 μmol/l DHE (Invitrogen) in PBS containing 1% (weight/vol) BSA at 37°C for 5 min; the stained area was quantified in six randomly selected microscopic fields (×20) per well using the ImageJ software.

Quantitative real-time PCR

RNA was isolated from mouse liver and IHHs with the EZNA Total RNA kit (R6834; Omega Bio-Tek, Norcross, GA) according to the manufacturer's recommendations. cDNA was synthesized using the high-capacity CDNA Reverse transcription kit (4368814; Applied Biosystems, Foster City, CA). Relative quantification was performed with the QuantStudio 6 Flex system (Applied Biosystems) or the CFX Connect real-time system (Bio-Rad). Relative quantities of target transcripts were calculated after normalization of the data to the endogenous control, 18S rRNA (Applied Biosystems).

Western blot

Western blot was performed as previously described (29) (see supplemental Table S1 for antibody information).

Ubiquitin pulldown assay

The ubiquitinated protein enrichment kit (662200; Calbiochem, San Diego, CA) was used according to the manufacturer's instructions. In brief, 200 μg of total protein lysate was tumbled with 40 μl affinity bead suspension overnight at 4°C. After the beads were washed three times in lysis buffer, the sample buffer was added, and the beads were incubated for 5 min at 95°C. Bound proteins were separated by gel electrophoresis and analyzed by Western blot using anti-catalase antibody (see supplemental Table S1).

Statistical analysis

Statistical significance between the groups was evaluated using the two-sample Student's *t*-test, and among more than two groups by one-way ANOVA followed by a two-sample Student's *t*-test for post hoc analysis, with a value of $P < 0.05$ considered statistically significant. All the reported *P* values are unadjusted for multiplicity. All statistical analyses were performed using Perseus software (30) or SPSS statistics (v24; IBM Corporation, Armonk, NY).

RESULTS

Our previous studies have demonstrated that reduced STK25 activity achieved either by genetic depletion or by ASO treatment efficiently prevents diet-induced NAFLD in mice (10–12, 14, 15). However, the mechanism-of-action of STK25 in hepatocytes and its molecular substrates have remained elusive. To identify downstream mediators of STK25 in regulation of NAFLD progression in an unbiased manner, we performed global quantitative phosphoproteomic analysis by a LC-MS technique on LDs isolated from freshly excised livers of high-fat diet-fed *Stk25* knockout mice and their wild-type littermates (**Fig. 1A**).

Following LC-MS analysis, we identified a total of 29,523 distinct peptides, corresponding to 4,515 unique proteins, in the liver LD fraction of high-fat diet-fed mice (Fig. 1B, C; supplemental Table S2). The LD fraction contained several expected bona fide LD marker proteins, such as PLIN2 (also known as ADRP or adipophilin), which is the most abundant hepatic LD-coating protein, and key regulators of lipid partitioning in LDs [ATGL (also known as PNPLA2), CGI-58 (also known as ABHD5), CIDEB, CES3, and RAB7] (5). Western blot analysis also confirmed that the LD fraction was highly enriched for the LD marker protein STK25 over its levels in the starting homogenate (i.e., postnuclear fraction), whereas we were unable to detect common cytosolic contaminating protein GAPDH in the LD fraction (supplemental Fig. S1). Although the LD fraction isolated by the sucrose centrifugation method, as was used in this study, has also previously been shown to be highly enriched for the LD-coating proteins, this method does not effectively deplete the peroxisomes, which copurify with the LD fraction (7, 18). Furthermore, morphological studies show LDs in close proximity to and interacting with several membrane-bound cellular organelles, including the ER, mitochondria, peroxisomes, and endosomes; because of these close associations, it is difficult to purify LDs to homogeneity (7, 8, 18, 31, 32). Thus, the proteins isolated in this study do not necessarily represent bona fide LD proteins residing primarily or exclusively on the LDs, and we therefore refer to them as "LD-associated proteins".

We compared the UniProt accession numbers of the LD-associated proteins identified in our analysis with the two recent proteomic studies performed on the LD fraction isolated from mouse liver homogenates by sucrose gradient centrifugation (7, 8). Crunk et al. (8) identified in total 149 LD-associated proteins in the liver of C57BL/6 mice that were fasted and then refed with low-fat or high-fat diet for 16 h. Khan et al. (7) identified in total 1,518 LD-associated proteins in the livers of C57BL/6J mice fed a normal chow or a 60% fat diet for 9 weeks. We found that 130 (87.2%) and 1,127 (74.2%) of the proteins detected in previous studies by Crunk et al. and Khan et al., respectively, were also represented in our analysis (supplemental Table S2). Furthermore, 101 out of 145 (67.7%) LD-associated proteins previously detected in human liver (33) were identified in our analysis (supplemental Table S2).

We observed that the abundance of 938 peptides representing 131 unique proteins was differentially regulated by

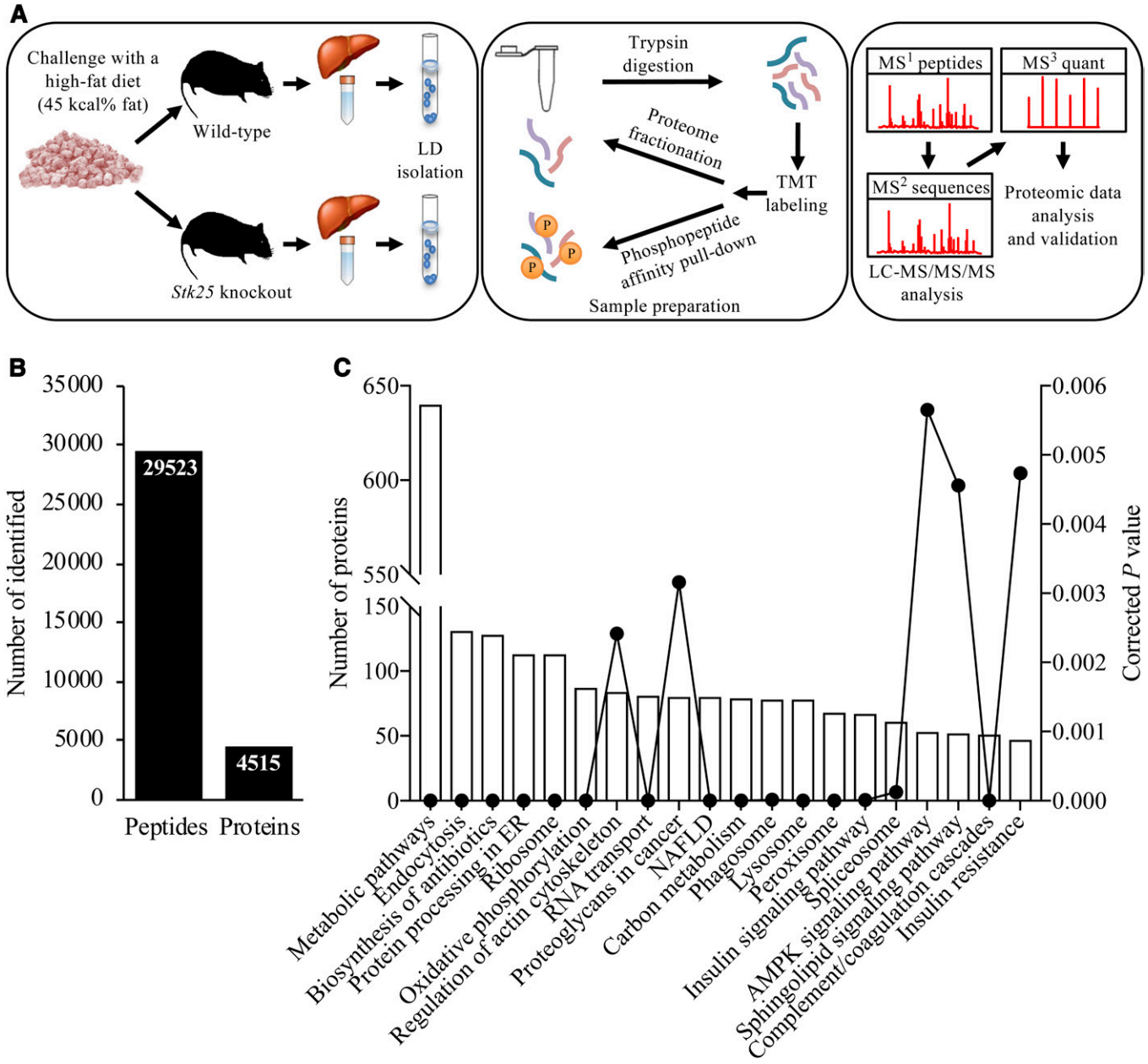

Fig. 1. Analysis of the hepatic LD-associated proteome in *Stk25* knockout mice and wild-type controls after chronic exposure to dietary lipids. A: Schematic presentation of the experimental design of the LC-MS analysis. LDs were isolated from the livers of high-fat diet-fed *Stk25*$^{-/-}$ and wild-type mice; the proteins were extracted and digested into peptides. The peptides were labeled with TMT reagents and then combined into one TMT 10-plex set. For the total proteome, the TMT-set was separated into eight fractions using high-pH LC and then subjected to online LC-MS analysis. Another part of the TMT-set was processed with phosphopeptide affinity columns and then analyzed with LC-MS using the Orbitrap Fusion Tribrid. Peptides were separated during 90 min, continuously mass measured, and then selected for fragmentation in MS2 using collision-induced dissociation ion trap for sequence identification while further fragmentation (MS3) to detect the TMT label and quantitation was performed in parallel in the Orbitrap. B: The total number of unique peptides and proteins identified in LC-MS analysis. C: Ontology analysis of identified LD-associated proteins. Corrected *P* value was calculated using a modified Fisher's exact test by DAVID (DAVID.ncifcrf.gov). AMPK, AMP-activated protein kinase.

a factor of 1.5-fold or more ($P < 0.05$) in the liver LDs of high-fat diet-fed *Stk25* knockout mice relative to their wild-type littermates (**Fig. 2A**, B; supplemental Table S3). Enrichment analysis of differentially represented LD-associated proteins by KEGG revealed that the two most robustly changed pathways in response to STK25 depletion were related to peroxisomal function and ubiquitin-mediated proteolysis (13 out of 29 proteins in the Metabolic pathways category and 7 out of 9 proteins in the PPAR signaling pathway category overlapped with the proteins in the Peroxisome category; Fig. 2C). Notably, the level of all differentially represented proteins related to peroxisomal function was coordinately downregulated, while the level of all proteins identified in the ubiquitin-mediated proteolysis pathway was upregulated in *Stk25*$^{-/-}$ livers (Fig. 2D). Consistent with the detection of peroxisomal proteins in

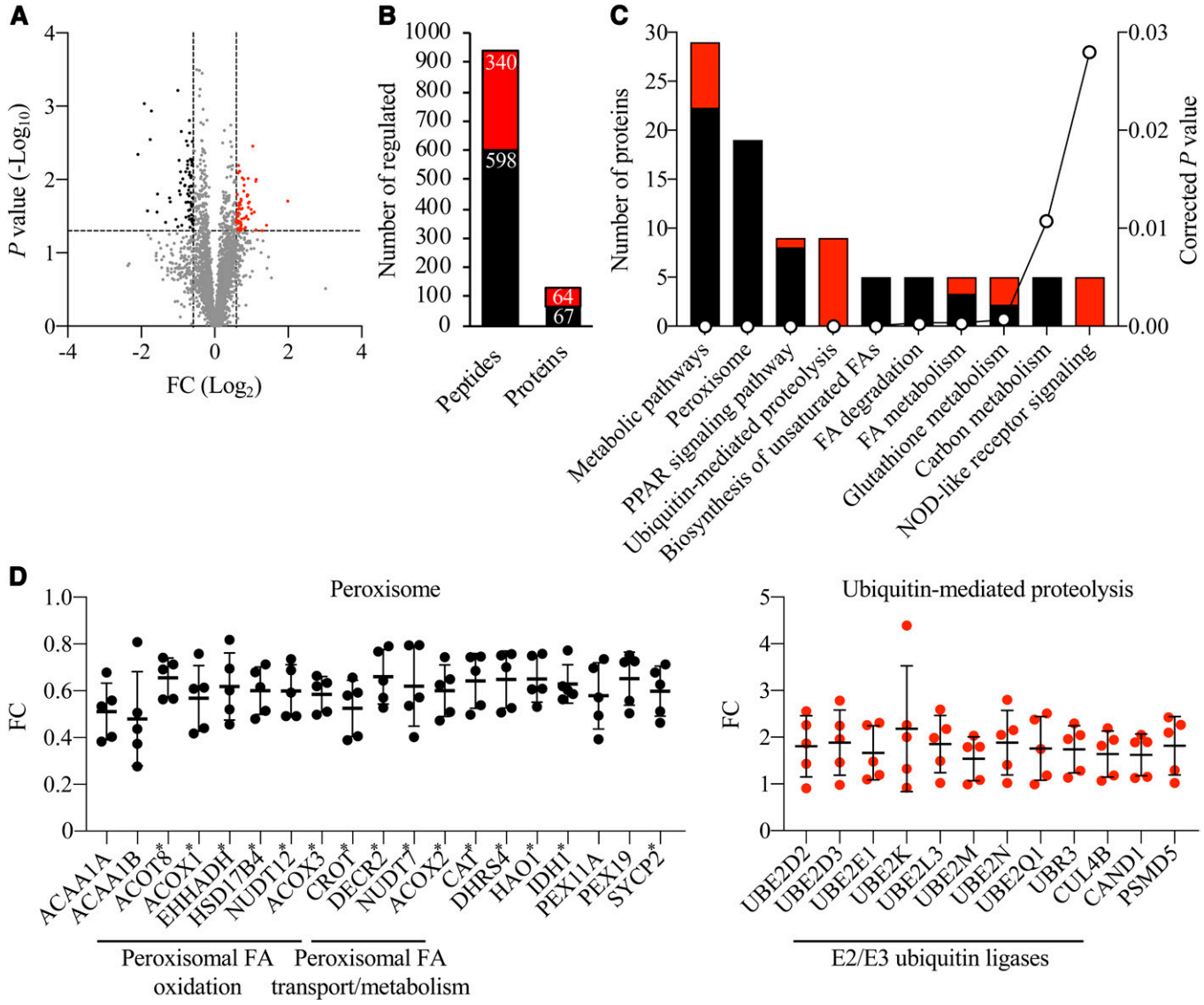

Fig. 2. Analysis of differentially represented proteins in *Stk25*$^{-/-}$ versus wild-type livers. A: Volcano plot of differentially represented LD-associated proteins. A ratio of 1.50-fold (vertical dashed lines) and a *P* value of 0.05 (horizontal dashed line) serve as the threshold for differential expression. B: The total number of differentially expressed unique peptides and proteins. C: Ontology analysis of differentially represented LD-associated proteins. The corrected *P* value was calculated using a modified Fisher's exact test by DAVID (DAVID.ncifcrf.gov). D: Relative abundance of individual differentially expressed peroxisomal proteins and components of the ubiquitin-mediated proteolysis pathway. Peroxisomal proteins containing a known or suspected PTS1 sequence (40–43) are indicated by asterisks. A–D: The red and black colors represent peptides/proteins, which were up- or downregulated in abundance, respectively, in *Stk25*$^{-/-}$ versus wild-type livers. FC, fold change.

LC-MS analysis, we found LDs closely associated with peroxisomes in the liver sections from high-fat diet-fed mice, which was evident both in *Stk25*$^{-/-}$ and wild-type livers (LDs and peroxisomes were visualized by immunofluorescence microscopy using antibodies against the main LD-coating protein, PLIN2, and the peroxisomal membrane marker, PMP70, respectively; supplemental Fig. S2).

STK25 is a Ste20-type serine/threonine kinase (9) and it is anticipated to carry out its functions at least partly via phosphorylating the downstream targets. We found that the phosphorylation level of 67 peptides derived from 60 unique proteins was differentially regulated by a factor of 1.5-fold or more ($P < 0.05$) when comparing the genotypes (**Fig. 3A**, B; supplemental Table S4; see also supplemental Table S5 for all phosphopeptide sequences identified). To identify changes in phosphopeptides not driven by underlying changes in the overall abundance of individual proteins, we performed correction of phosphopeptide levels with total protein levels (Fig. 3C). This analysis identified 12 peptides with reduced phosphorylation status in *Stk25*$^{-/-}$ livers, representing potential target sites for the kinase activity of STK25 (Fig. 3D, supplemental Table S4). Comparison of the phosphosites that were downregulated in *Stk25*$^{-/-}$ livers using the BlockLogo application (34) identified a consensus sequence with a high variability in most positions, although a proline-directed ([pS]P) motif was over-represented (Fig. 3E). Importantly, because the STK25 protein is globally depleted early in development in

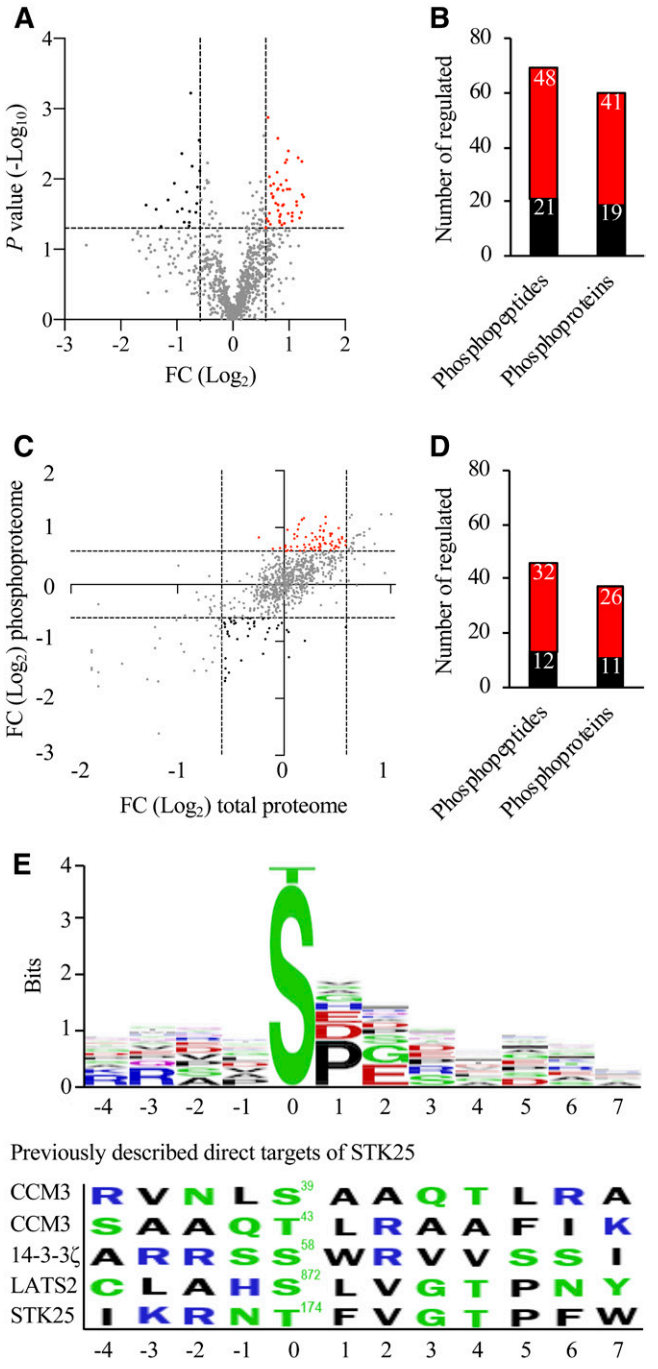

Fig. 3. Analysis of differentially phosphorylated proteins in *Stk25*$^{-/-}$ versus wild-type livers. A: Volcano plot of differentially phosphorylated LD-associated proteins. A ratio of 1.50-fold (vertical dashed lines) and a *P* value of 0.05 (horizontal dashed line) serve as the threshold for differential phosphorylation. B: The total number of differentially phosphorylated unique peptides and proteins. C: To identify changes in phosphopeptide abundance that were not driven by underlying changes in the abundance of corresponding proteins, the following thresholds were applied: change in total protein abundance <1.50-fold; change in phosphosite >1.50-fold (dashed lines). D: The total number of unique peptides and proteins with a significant change in phosphorylation levels but not in the total protein levels. A–D: The red and black colors represent peptides/proteins, which were up- or downregulated at phosphorylation level, respectively, in *Stk25*$^{-/-}$ versus wild-type livers. E: Consensus sequences were extracted from the peptides with downregulated phosphorylation events in *Stk25* knockout livers compared with wild-type livers using the BlockLogo application (34). The residue position in relation to the phosphorylation site is shown on the x-axis and the information content is shown on the y-axis, where the height of the logo element represents its log transformed frequency displayed in bits of information. The colors of the amino acids correspond to their chemical properties; polar amino acids (G, S, T, Y, C, Q, and N) are shown in green, basic amino acids (K, R, and H) are shown in blue, acidic amino acids (D and E) are shown in red, and hydrophobic amino acids (A, V, L, I, P, W, F, and M) are shown in black. The phosphorylation sites of the previously described direct targets of STK25 [Ser^{39}/Thr^{43} in CCM3, Ser^{58} in 14-3-3ζ, Ser^{872} in LATS2, and Thr^{174} in STK25 (36–38)] are shown for comparison. FC, fold change.

knockout mice (35), it is not possible to discriminate between direct and indirect targets of STK25 activity using this conventional model of gene inactivation. Notably, we could not detect any conserved motifs when we aligned the consensus sequence extracted from the peptides with downregulated phosphorylation events in *Stk25* knockout livers identified in our study with the phosphorylation sites of the previously described direct targets of STK25 [Ser^{39}/Thr^{43} in CCM3, Ser^{58} in 14-3-3ζ, Ser^{872} in LATS2, and Thr^{174} in STK25 (36–38)] (Fig. 3E). This observation is consistent with the interpretation that the changes in phosphorylation pattern of the LD-associated proteins from *Stk25* knockout versus wild-type livers are likely not caused, or at least not solely caused, by a direct effect of STK25 kinase activity. KEGG analysis on differentially phosphorylated proteins did not reveal any significantly enriched pathways.

Interestingly, a majority of peroxisomal proteins, which were decreased in abundance in the liver LD fraction of *Stk25*$^{-/-}$ mice (Fig. 2D), are known or putative PPARα targets in the liver (39, 40). We therefore determined the hepatic mRNA levels of selected differentially represented peroxisomal proteins, which are known targets of PPARα signaling, in mice fed a high-fat diet. No decrease in mRNA abundance was detected for any of the selected genes in *Stk25*$^{-/-}$ versus wild-type livers (supplemental Fig. S3), suggesting that the suppression in peroxisomal protein abundance observed in the hepatic LD fraction of *Stk25* knockout mice was not regulated at the transcriptional level. Notably, we have previously analyzed a panel of hepatic mRNA transcripts of genes involved in glucose and lipid metabolism in high-fat diet-fed *Stk25*$^{-/-}$ and wild-type mice (10), and a number of genes included in this panel are also well-known PPARα targets in the liver [*Acaca*, *Acacb*, *Acox1*, *Fasn*, *G6pc*, *Gpam*, *Lpl*, *Pck1*, *Scd1*, *Srebf1*, and *Ucp3* (39)]. Consistent with the results of the current study, we did not detect any difference in the expression levels of these genes in *Stk25*$^{-/-}$ livers compared with wild-type livers (10). Taken together, the analysis of mRNA expression argues against reduced hepatic PPARα signaling in response to STK25 depletion.

Nearly all peroxisomal proteins, which were downregulated in the livers from *Stk25*$^{-/-}$ mice, contain a known or suspected peroxisomal targeting signal 1 (PTS1) (Fig. 2D), a short carboxy-terminal sequence specifically recognized

by the receptor protein PEX5 (41–44). PEX5 binds PTS1-carrying proteins in the cytosol delivering them to the peroxisomal import system; PEX5 deficiency in mice and humans leads to the structural and functional defects in peroxisomes (so called ghost peroxisomes) due to the inability to import matrix proteins into peroxisomes (44–46). Interestingly, we found that immunostaining for PEX5 was also 1.8 ± 0.2-fold suppressed in the livers from high-fat diet-fed *Stk25* knockout mice compared with wild-type controls (**Fig. 4**), suggesting that a defect in peroxisomal biogenesis due to reduced PEX5 levels may have contributed to the decrease in peroxisomal protein abundance observed in the liver LD fraction of *Stk25*$^{-/-}$ mice. Notably, the depletion of STK25 in knockout mice did not result in hepatic accumulation of peroxisomal β-oxidation substrates such as VLCFAs (carbon chain length greater than 22), or in liver deficiency of plasmalogens, which are synthesized in peroxisomes (supplemental Fig. S4).

To confirm the changes in the two most robustly regulated pathways revealed by LC-MS analysis in the livers from *Stk25*$^{-/-}$ versus wild-type mice, we studied the peroxisomal function and ubiquitin-mediated proteolysis in human hepatocytes transfected with *STK25*-specific siRNA or with a nontargeting control (NTC) siRNA. In IHHs transfected with *STK25* siRNA, the target mRNA expression was repressed by approximately 90% (supplemental Fig. S5), whereas the protein abundance of STK25 was below the detection limit of Western blot. In all cell experiments described below, we exposed the transfected hepatocytes to oleic acid, known to efficiently induce steatosis in vitro (47–51), in order to mimic conditions in obese mice and in high-risk individuals. In line with coordinately reduced abundance of peroxisomal proteins in the livers from *Stk25*$^{-/-}$ mice, we found that immunostaining for peroxisome biogenesis marker PEX5 was more than 2-fold suppressed in STK25-deficient IHHs (**Fig. 5A**). Interestingly, Western blot analysis of total protein lysates using anti-ubiquitin antibody did not reveal any differences in the overall abundance of ubiquitinated proteins comparing IHHs transfected with *STK25* siRNA versus NTC siRNA (supplemental Fig. S6A) or livers from *Stk25*$^{-/-}$ versus wild-type mice (supplemental Fig. S6B). LDs have been postulated to act as reservoirs for unfolded proteins (52), and it is therefore possible that only proteins in the ubiquitin-mediated proteolysis pathway, which are represented in the LD fraction of the liver lysate, were increased in *Stk25* knockout mice compared with wild-type littermates.

To study the ubiquitin-mediated proteasome degradation of peroxisomal proteins specifically, we focused on catalase, which is one of the most abundant peroxisomal proteins known to be targeted to the peroxisomal matrix by PEX5 via its PTS1 motif (53). Consistent with the results of LC-MS analysis revealing lower catalase levels in the liver LD fraction of *Stk25*$^{-/-}$ mice (Fig. 2D), we found that immunostaining for catalase was 1.6 ± 0.1-fold suppressed in IHHs transfected with *STK25* siRNA compared with NTC siRNA (supplemental Fig. S7). Notably, lower catalase levels were detected in STK25-deficient IHHs even in the presence of proteasome inhibitor MG132 (supplemental Fig. S7). Interestingly, in spite of the similar overall ubiquitination pattern observed (supplemental Fig. S6), the relative abundance of ubiquitinated catalase was 1.6 ± 0.2-fold higher in IHHs transfected with *STK25* siRNA versus NTC siRNA (supplemental Fig. S8).

LC-MS analysis also revealed that the protein abundance of several key mediators of hepatic metabolic stress and lipid homeostasis, fatty acid binding protein (FABP1), glutathione s-transferase theta (GSTT2 and GSTT3), and CIDEA, was significantly changed in the livers from *Stk25*$^{-/-}$ versus wild-type mice. Consistently, we found that the total protein level of FABP1 and GSTT2 was 2.8 ± 0.4- and 1.3 ± 0.1-fold higher, respectively, whereas the protein abundance of CIDEA was 1.4 ± 0.1-fold lower, when assessed by Western blot in IHHs transfected with *STK25* siRNA versus NTC siRNA (no human ortholog is reported for GSTT3; **Fig. 6A**). Interestingly, *FABP1* mRNA expression was also markedly increased in response to STK25 depletion in IHHs (supplemental Fig. S5).

Reduced peroxisomal activity and an increase in the cytoprotective enzymes, FABP1 and GSTT2/GSTT3, in STK25-deficient hepatocytes is expected to protect the cells against oxidative and ER stress. Indeed, the staining for 4-HNE, an end product of peroxidation of membrane *N*-6-polyunsaturated fatty acids and considered a reliable biomarker of oxidative damage in hepatocytes, and for the dye DHE, which quantifies superoxide radicals ($O_2^{\bullet -}$), was 3.9 ± 0.4- and 2.4 ± 0.3-fold reduced, respectively, in IHHs transfected with *STK25* siRNA compared with NTC siRNA (Fig. 5B, C). We also found significantly lower mRNA levels of the major indicators of ER stress, *CHOP* (also known as *DDIT3*), *BIP* (also known as *HSPA5* or *GRP78*), and *ATF4*, in STK25-deficient hepatocytes (**Fig. 7**). Suppressed immunostaining for KDEL, a well-characterized ER stress marker, also supports protection against ER stress in hepatocytes where STK25 was depleted (Fig. 5D). Furthermore, the mRNA expression of the pro-apoptotic markers *BAX* and caspase 3 (*CASP3*) was significantly lower in IHHs transfected with *STK25* siRNA (Fig. 7), which is consistent with the

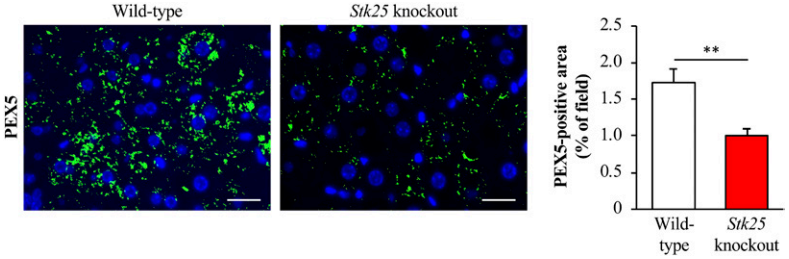

Fig. 4. Analysis of immunostaining for peroxisomal biogenesis marker PEX5 in *Stk25*$^{-/-}$ versus wild-type livers. Representative liver sections processed for immunofluorescence with anti-PEX5 antibody (green); nuclei stained with DAPI (blue). Scale bars, 20 μm. Quantification of PEX5 staining. Results are the mean ± SEM from six mice per group. $^{**}P < 0.01$ comparing the liver sections from high-fat diet-fed *Stk25*$^{-/-}$ versus wild-type mice.

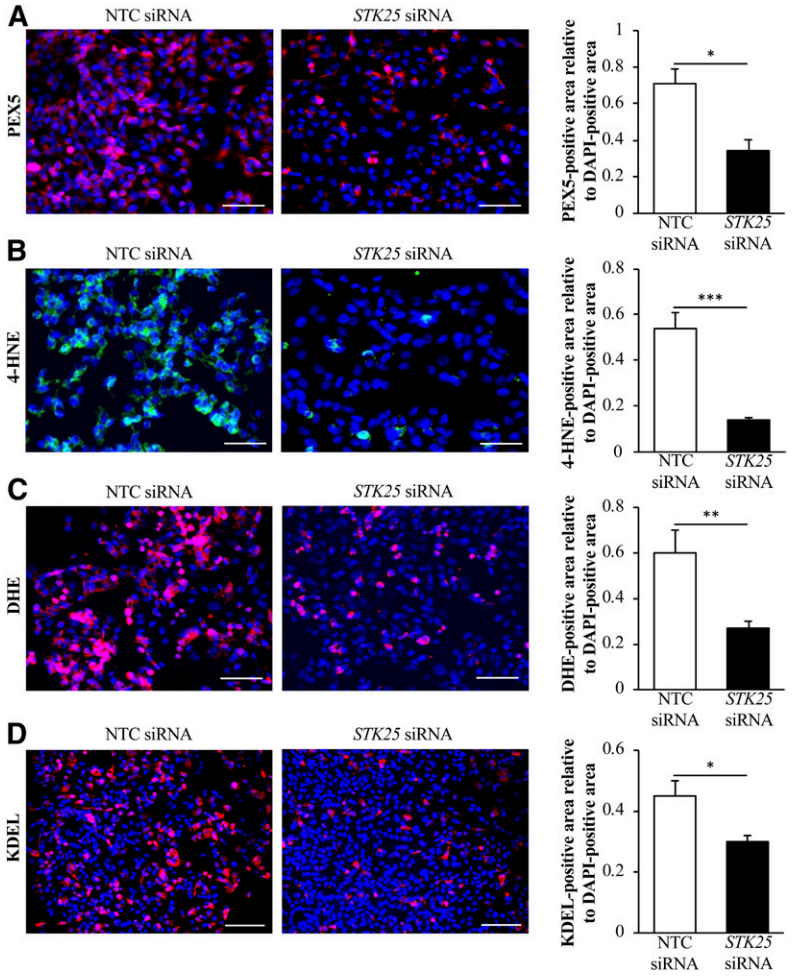

Fig. 5. Assessment of peroxisomal biogenesis as well as oxidative and ER stress in human hepatocytes in which STK25 was depleted. IHHs were transfected with *STK25* siRNA or NTC siRNA and challenged with oleic acid for 48 h. Representative images of cells processed for immunofluorescence with anti-PEX5 antibody (pink; A), anti-4-HNE antibody (green; B), or anti-KDEL antibody (pink, *D*), or stained with DHE (pink, C); nuclei stained with DAPI (blue). Scale bars, 40 μm (A–C) or 60 μm (D). Quantification of PEX5 (A), 4-HNE (B), DHE (C), and KDEL (D) staining. Results are the mean ± SEM from six wells per test condition. $*P < 0.05$, $**P < 0.01$, and $***P < 0.001$ comparing cells transfected with *STK25* siRNA versus NTC siRNA.

aggravated oxidative and ER stress accelerating hepatocyte apoptosis in cells transfected with NTC siRNA (54). Activated c-Jun-N-terminal kinase (JNK) (phospho-JNK Thr^{183}/Tyr^{185}), which is an important downstream mediator of ER stress-associated lipo-apoptosis and has been implicated in human and murine steatohepatitis (55, 56), was also markedly reduced in STK25-deficient hepatocytes (Fig. 6B).

DISCUSSION

In this study, we provide a nonbiased quantitative profiling of changes in the liver LD-associated proteome in high-fat diet-fed *Stk25* knockout mice versus wild-type littermates by LC-MS technique. The majority of proteins that have been previously reported in liver LD proteomic analyses (7, 8, 33) were also identified in our study. However, our analysis detected a higher total number of LD-associated proteins compared with previous reports, which likely relates to the differences in instrumentation. Compared with the mass spectrometers used in these previous studies for LC-MS analysis [Velos Orbitrap (7) or LTQ XL mass spectrometers (8, 33)], the instrument used in our study (Orbitrap Fusion Tribrid mass spectrometer) is faster in data acquisition with higher MSn scanning rates, wide dynamic range, and ultrahigh mass resolution, which provides a higher sensitivity when detecting peptides with low abundance. As an example, we identified two low-abundance proteins in our LD preparation, Ste20-type kinases MST3 and STK25, which were not detected in these previous studies (7, 8, 33). Both MST3 and STK25 have also been shown to localize to the LD surface by immunostaining of mouse liver sections and human cultured hepatocytes (11, 13, 57).

Importantly, the proteins detected in this study can reside solely or partly in liver LDs but they can also reside in organelles that tightly associate with LDs, such as peroxisomes, ER, mitochondria, and endosomes. Thus, although our study provides a characterization of liver proteomics enriched for LD proteins, the current analysis (as any proteomic study) does not discriminate between bona fide LD proteins and contaminant proteins residing in peroxisomes or other copurifying organelles.

Our previous studies have revealed that STK25 coats intracellular LDs in mouse and human hepatocytes (11, 13). We also found that knockdown of STK25 protects liver cells from ectopic lipid deposition within LDs by enhancing lipolysis, and thereby releasing free fatty acids for β-oxidation and VLDL-TAG secretion, and by reducing the rate of lipid synthesis (10, 13). Based on these findings, it is attractive to hypothesize that STK25 regulates liver lipid homeostasis locally in LDs by controlling the abundance, activity,

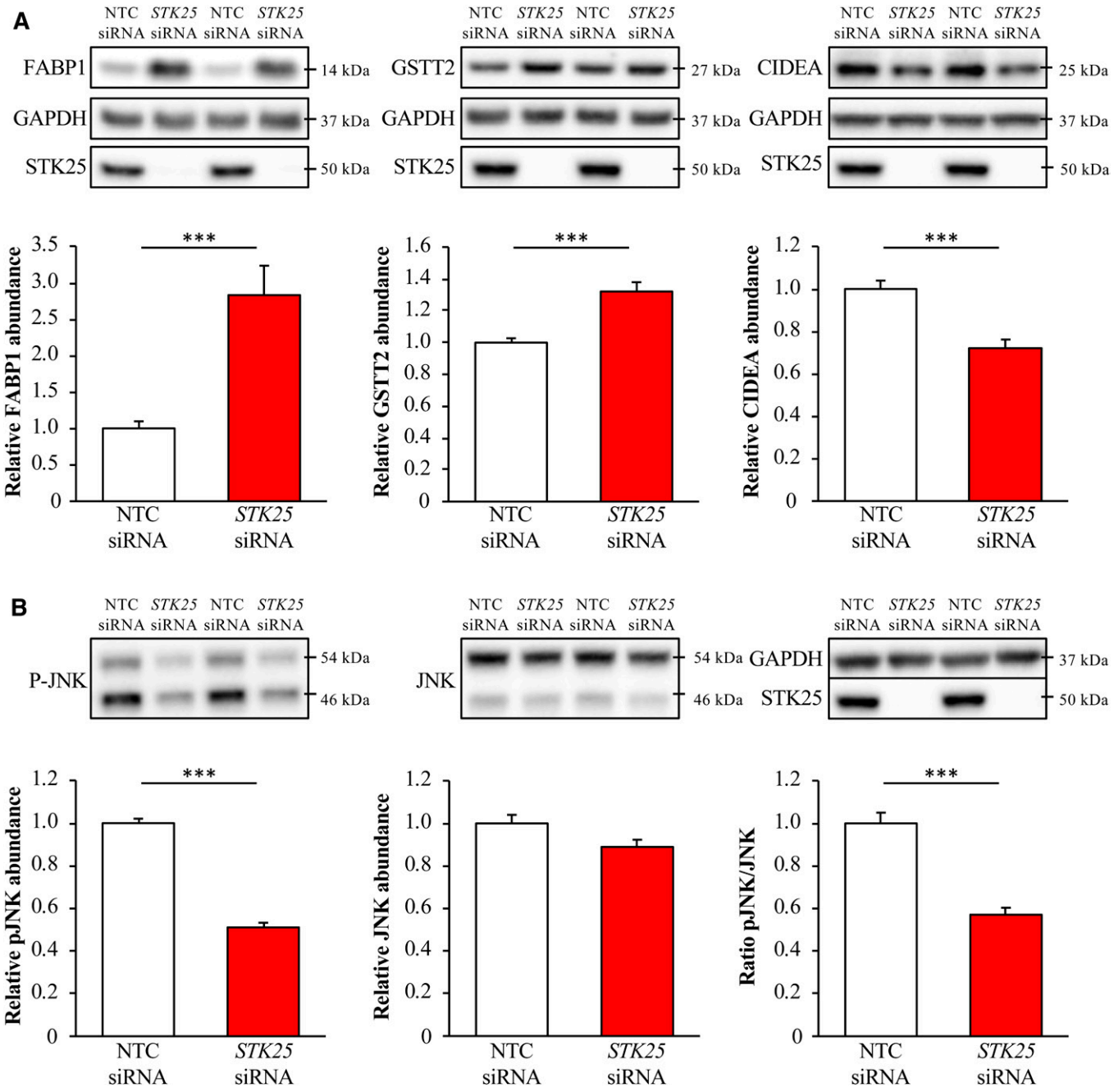

Fig. 6. Measurement of protein abundance in STK25-deficient human hepatocytes. IHHs were transfected with *STK25* siRNA or NTC siRNA and challenged with oleic acid for 48 h. Cell lysates were analyzed by Western blot using antibodies specific for FABP1, GSTT2, and CIDEA (A), phospho-JNK (Thr^{183}/Tyr^{185}) and JNK (B), or STK25 (A, B). Representative Western blots are shown with GAPDH used as a loading control. Protein levels were analyzed by densitometry and data are shown as the protein abundance for FABP1, GSTT2, CIDEA, JNK, and phospho-JNK as well as the ratio of phospho-JNK/total JNK. Results are the mean ± SEM from 11–12 wells per test condition. ***$P < 0.001$ comparing cells transfected with *STK25* siRNA versus NTC siRNA.

and/or subcellular localization of LD-associated lipases and enzymes for TAG and phospholipid synthesis. However, global proteomic analysis did not detect any significant differences in the total protein abundance or the phosphorylation pattern of known LD-associated lipases or lipid synthesis enzymes in *Stk25* knockout livers. Interestingly, LC-MS analysis revealed that a number of proteins involved in peroxisomal function were coordinately suppressed in the livers from high-fat diet-fed $Stk25^{-/-}$ mice versus wild-type controls, including mediators of peroxisomal fatty acid transport, metabolism, and β-oxidation. As explained above, we do not believe that these peroxisomal proteins were differentially represented on the hepatic LDs from $Stk25^{-/-}$ mice, or that the interactions between LDs and peroxisomes differed comparing the genotypes, but rather that *Stk25* knockout livers displayed reduced activity of peroxisomes, which then copurified with the LD fraction. Consistent with this interpretation, we also found suppressed immunostaining for peroxisomal biogenesis marker PEX5 in the liver sections from high-fat diet-fed

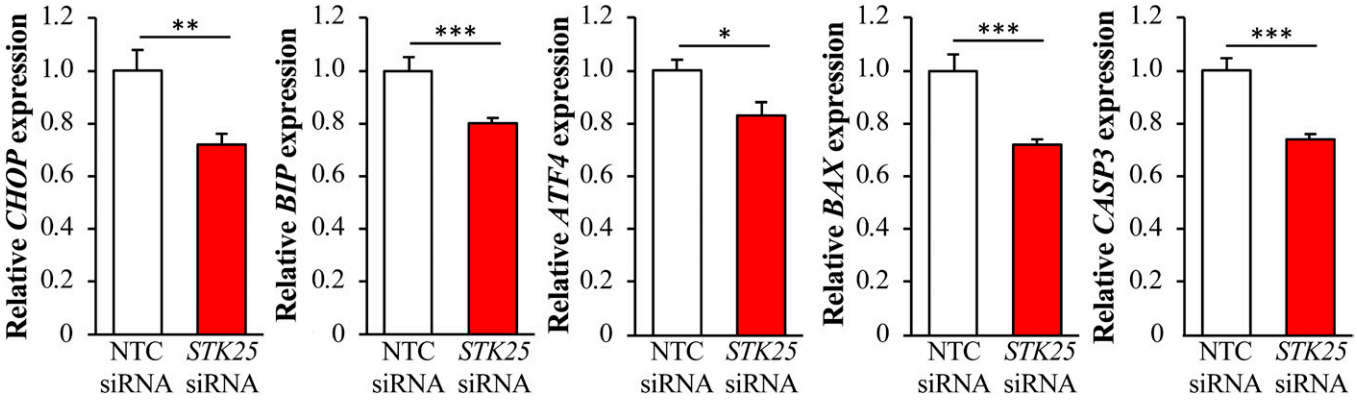

Fig. 7. Measurement of the mRNA expression of selected markers for ER stress and hepatocellular apoptosis in STK25-deficient human hepatocytes. IHHs were transfected with *STK25* siRNA or NTC siRNA and challenged with oleic acid for 48 h. Relative mRNA expression was assessed by quantitative real-time PCR. Results are the mean ± SEM from eight wells per test condition. *$P < 0.05$, **$P < 0.01$, and ***$P < 0.001$ comparing cells transfected with *STK25* siRNA versus NTC siRNA.

Stk25$^{-/-}$ mice and in STK25-deficient human hepatocytes cultured under the conditions of increased metabolic stress.

In line with copurification of LDs and peroxisomes in our LC-MS analysis, we here found LDs (visualized by PLIN2 immunostaining) closely associated with peroxisomes (visualized by PMP70 immunostaining) in the liver sections from high-fat diet-fed *Stk25*$^{-/-}$ and wild-type mice. Our previous investigations in the livers of high-fat diet-fed mice have shown that STK25 fully colocalizes with the main hepatic LD-coating protein PLIN2 (11). However, due to the high degree of colocalization of PLIN2 and PMP70 in steatotic liver, it has not been possible to convincingly conclude by using immunofluorescence microscopy whether STK25 only localizes to the LDs or is also present in the peroxisomal subpopulation. Notably, we found no peroxisomal localization motifs in STK25 protein sequence using the PTS1 Predictor, the most cited prediction model for peroxisome targeting (58, 59). Furthermore, to our knowledge, STK25 has not been identified among peroxisomal proteins by any quantitative or nonquantitative proteomic studies or by entries in the UniProtKB and Compartments knowledge channel databases (60).

Lipid overload and/or compromised mitochondrial function in hepatocytes in NAFLD are known to force a higher degree of fatty acid oxidation to take place in the peroxisomes, leading to excessive oxidative stress, which in turn aggravates ER stress and promotes liver inflammation, fibrosis, and hepatocellular apoptosis, thus triggering the disease progression toward NASH (61, 62). In line with lower peroxisomal activity in STK25-deficient hepatocytes reported in this study, we have previously described protection against diet-induced oxidative stress accompanied by reduced inflammatory infiltration, nutritional fibrosis, and apoptosis in the livers from *Stk25*$^{-/-}$ mice and mice treated with *Stk25* ASOs when compared with control groups of mice (12, 14, 15). Furthermore, in this study, we also found evidence of suppressed oxidative and ER stress as well as reduced expression of apoptosis markers in human hepatocytes where STK25 was depleted. Taken together, these findings suggest that reduced peroxisomal activity in STK25-deficient hepatocytes, accompanied by suppressed oxidative and ER stress, may play a crucial role in protection against NASH previously observed in mice with repressed STK25 activity (12, 14, 15).

LC-MS analysis in this study also revealed increased protein abundance of several mediators, which are well-documented to be tightly linked to protection against oxidative stress (GSTT2, GSTT3, and FABP1) (63–68), in the livers from high-fat diet-fed *Stk25*$^{-/-}$ mice, and this observation was confirmed in STK25-deficient human hepatocytes. Thus, the inhibition of STK25 may suppress hepatic oxidative stress both by reducing the formation of reactive oxygen species in peroxisomes and by augmenting liver antioxidant defense.

Notably, FABP1 is the most prevalent lipid chaperone in liver cytosol, and in vitro studies in cultured cells have shown that FABP1 is critical for the uptake and peroxisomal oxidation of branched-chain fatty acids (69–71). FABP1 has even been detected within peroxisomes and it has been suggested that this protein may not only chaperone bound branched-chain fatty acyl-CoA to peroxisomes but also to oxidative enzymes within peroxisomes (60, 72). Although the action of FABP is closely related to peroxisomal function, it is unlikely that the elevated FABP1 levels seen in STK25-deficient hepatocytes are directly linked to the loss of peroxisomal proteins, inasmuch as FABP1 typically coincides with increased peroxisomal activity.

Interestingly, we found a lower protein abundance of CIDEA in the livers from *Stk25*$^{-/-}$ mice and in human hepatocytes transfected with *STK25* siRNA. CIDEA localizes to LD-LD contact sites to promote LD fusion in hepatocytes (73), and the knockdown of CIDEA in the livers of obese mice alleviates hepatic steatosis and reduces the size of intrahepatocellular LDs (74, 75). Furthermore, *CIDEA* expression highly correlates with the severity of NAFLD in humans (74). Thus, the suppression of CIDEA abundance reported in this study could be part of the mechanism behind the previously reported reduction in ectopic lipid deposition in STK25-deficient hepatocytes (10, 12–15).

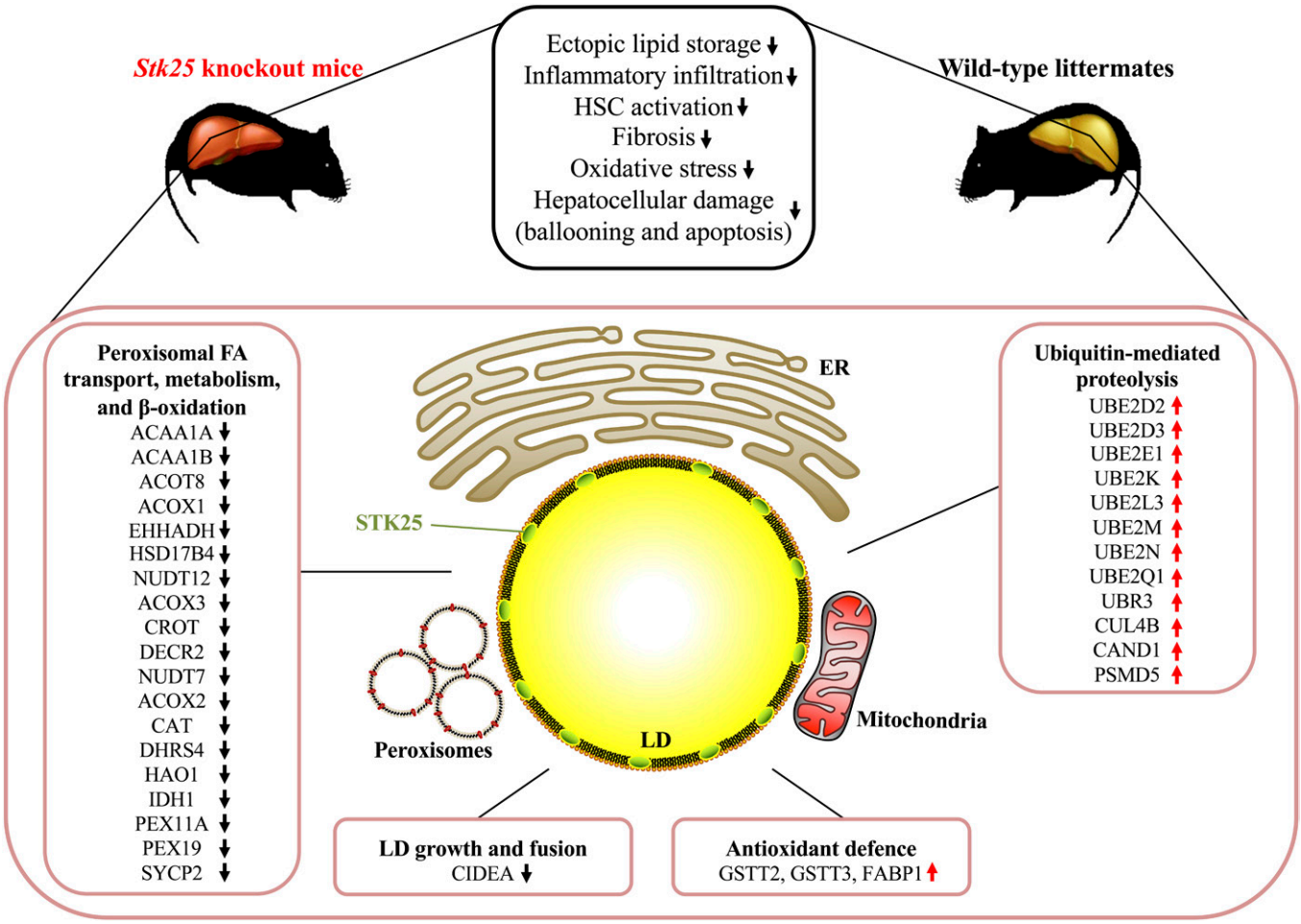

Fig. 8. Schematic illustration of metabolic responses and molecular-level differences in the livers from *Stk25* knockout mice compared with wild-type controls. Phenotypic differences in the livers from Stk25$^{-/-}$ versus wild-type mice are based on our previous publications (10, 12). HSC, hepatic stellate cell.

Currently, we do not understand the mechanisms of how STK25 regulates the abundance of the differentially represented proteins. Interestingly, similarly to the FABP1 protein, the expression of *FABP1* mRNA was increased several-fold in STK25-deficient human hepatocytes, suggesting that STK25 regulates this target at least partly through transcriptional control. This is consistent with global proteomic analyses presented by other research groups, which demonstrate that the proteins associated with LDs serve a range of complex functions including cell signaling, membrane trafficking, protein turnover, and transcriptional regulation (7, 8). In contrast to FABP1, the differences in peroxisomal protein abundance observed in the hepatic LD fraction of *Stk25*$^{-/-}$ versus wild-type mice were not regulated at the level of gene expression.

Of the 44 differentially regulated phosphopeptides detected in *Stk25*$^{-/-}$ livers, the exact phosphorylation site could be determined in 31 peptides, and 29 of those were annotated in PhosphoSitePlus (76). However, the functional implication of the phosphorylation at these sites has only been described for Ser^{1597} of eIF4G1, which is described as a target site for casein kinase 2-α (CK2-α)-mediated phosphorylation (77), and Ser^{153} of WRNIP1, which is known to represent bona fide target of MAPKs (78).

In summary, our analysis has comprehensively quantified the differences in hepatic LD-associated proteome in *Stk25* knockout mice compared with wild-type controls after chronic exposure to dietary lipids (**Fig. 8**). The results of the study suggest that changes in peroxisomal activity as well as oxidative and ER stress response play a crucial role in molecular mechanisms underlying the impact of STK25 on the development and progression of NAFLD/NASH.

The Proteomics Core Facility at Sahlgrenska Academy, University of Gothenburg performed the quantitative proteomic analysis. The Proteomics Core Facility is grateful to the I. B. and A. Lundbergs Research Foundation for the donation of the Orbitrap Fusion Tribrid mass spectrometer.

REFERENCES

1. Younossi, Z., Q. M. Anstee, M. Marietti, T. Hardy, L. Henry, M. Eslam, J. George, and E. Bugianesi. 2018. Global burden of NAFLD and NASH: trends, predictions, risk factors and prevention. *Nat. Rev. Gastroenterol. Hepatol.* **15:** 11–20.
2. Younossi, Z., M. Stepanova, J. P. Ong, I. M. Jacobson, E. Bugianesi, A. Duseja, Y. Eguchi, V. W. Wong, F. Negro, Y. Yilmaz, et al.; Global Nonalcoholic Steatohepatitis Council. 2019. Nonalcoholic steatohepatitis is the fastest growing cause of hepatocellular carcinoma

in liver transplant candidates. *Clin. Gastroenterol. Hepatol.* **17:** 748–755.e3.
3. Anstee, Q. M., G. Targher, and C. P. Day. 2013. Progression of NAFLD to diabetes mellitus, cardiovascular disease or cirrhosis. *Nat. Rev. Gastroenterol. Hepatol.* **10:** 330–344.
4. Younes, R., and E. Bugianesi. 2019. A spotlight on pathogenesis, interactions and novel therapeutic options in NAFLD. *Nat. Rev. Gastroenterol. Hepatol.* **16:** 80–82.
5. Mashek, D. G., S. A. Khan, A. Sathyanarayan, J. M. Ploeger, and M. P. Franklin. 2015. Hepatic lipid droplet biology: Getting to the root of fatty liver. *Hepatology.* **62:** 964–967.
6. Barbosa, A. D., and S. Siniossoglou. 2017. Function of lipid droplet-organelle interactions in lipid homeostasis. *Biochim. Biophys. Acta Mol. Cell Res.* **1864:** 1459–1468.
7. Khan, S. A., E. E. Wollaston-Hayden, T. W. Markowski, L. Higgins, and D. G. Mashek. 2015. Quantitative analysis of the murine lipid droplet-associated proteome during diet-induced hepatic steatosis. *J. Lipid Res.* **56:** 2260–2272.
8. Crunk, A. E., J. Monks, A. Murakami, M. Jackman, P. S. Maclean, M. Ladinsky, E. S. Bales, S. Cain, D. J. Orlicky, and J. L. McManaman. 2013. Dynamic regulation of hepatic lipid droplet properties by diet. *PLoS One.* **8:** e67631.
9. Thompson, B. J., and E. Sahai. 2015. MST kinases in development and disease. *J. Cell Biol.* **210:** 871–882.
10. Amrutkar, M., E. Cansby, U. Chursa, E. Nunez-Duran, B. Chanclon, M. Stahlman, V. Friden, L. Manneras-Holm, A. Wickman, U. Smith, et al. 2015. Genetic disruption of protein kinase STK25 ameliorates metabolic defects in a diet-induced type 2 diabetes model. *Diabetes.* **64:** 2791–2804.
11. Amrutkar, M., E. Cansby, E. Nunez-Duran, C. Pirazzi, M. Stahlman, E. Stenfeldt, U. Smith, J. Boren, and M. Mahlapuu. 2015. Protein kinase STK25 regulates hepatic lipid partitioning and progression of liver steatosis and NASH. *FASEB J.* **29:** 1564–1576.
12. Amrutkar, M., U. Chursa, M. Kern, E. Nunez-Duran, M. Stahlman, S. Sutt, J. Boren, B. R. Johansson, H. U. Marschall, M. Bluher, et al. 2016. STK25 is a critical determinant in nonalcoholic steatohepatitis. *FASEB J.* **30:** 3628–3643.
13. Amrutkar, M., M. Kern, E. Nunez-Duran, M. Stahlman, E. Cansby, U. Chursa, E. Stenfeldt, J. Boren, M. Bluher, and M. Mahlapuu. 2016. Protein kinase STK25 controls lipid partitioning in hepatocytes and correlates with liver fat content in humans. *Diabetologia.* **59:** 341–353.
14. Nuñez-Durán, E., M. Aghajan, M. Amrutkar, S. Sutt, E. Cansby, S. L. Booten, A. Watt, M. Stahlman, N. Stefan, H. U. Haring, et al. 2017. Serine/threonine protein kinase 25 antisense oligonucleotide treatment reverses glucose intolerance, insulin resistance, and nonalcoholic fatty liver disease in mice. *Hepatol. Commun.* **2:** 69–83.
15. Cansby, E., E. Nunez-Duran, E. Magnusson, M. Amrutkar, S. L. Booten, N. M. Kulkarni, T. L. Svensson, J. Boren, H. U. Marschall, M. Aghajan, et al. 2019. Targeted delivery of Stk25 antisense oligonucleotides to hepatocytes protects mice against nonalcoholic fatty liver disease. *Cell. Mol. Gastroenterol. Hepatol.* **7:** 597–618.
16. Matsuki, T., R. T. Matthews, J. A. Cooper, M. P. van der Brug, M. R. Cookson, J. A. Hardy, E. C. Olson, and B. W. Howell. 2010. Reelin and stk25 have opposing roles in neuronal polarization and dendritic Golgi deployment. *Cell.* **143:** 826–836.
17. Ding, Y., S. Zhang, L. Yang, H. Na, P. Zhang, H. Zhang, Y. Wang, Y. Chen, J. Yu, C. Huo, et al. 2013. Isolating lipid droplets from multiple species. *Nat. Protoc.* **8:** 43–51.
18. Zhang, H., Y. Wang, J. Li, J. Yu, J. Pu, L. Li, H. Zhang, S. Zhang, G. Peng, F. Yang, et al. 2011. Proteome of skeletal muscle lipid droplet reveals association with mitochondria and apolipoprotein a-I. *J. Proteome Res.* **10:** 4757–4768.
19. Wiśniewski, J. R., A. Zougman, N. Nagaraj, and M. Mann. 2009. Universal sample preparation method for proteome analysis. *Nat. Methods.* **6:** 359–362.
20. Szklarczyk, D., A. Franceschini, S. Wyder, K. Forslund, D. Heller, J. Huerta-Cepas, M. Simonovic, A. Roth, A. Santos, K. P. Tsafou, et al. 2015. STRING v10: protein-protein interaction networks, integrated over the tree of life. *Nucleic Acids Res.* **43:** D447–D452.
21. Smoot, M. E., K. Ono, J. Ruscheinski, P. L. Wang, and T. Ideker. 2011. Cytoscape 2.8: new features for data integration and network visualization. *Bioinformatics.* **27:** 431–432.
22. Löfgren, L., M. Stahlman, G. B. Forsberg, S. Saarinen, R. Nilsson, and G. I. Hansson. 2012. The BUME method: a novel automated chloroform-free 96-well total lipid extraction method for blood plasma. *J. Lipid Res.* **53:** 1690–1700.
23. Ekroos, K., C. S. Ejsing, U. Bahr, M. Karas, K. Simons, and A. Shevchenko. 2003. Charting molecular composition of phosphatidylcholines by fatty acid scanning and ion trap MS3 fragmentation. *J. Lipid Res.* **44:** 2181–2192.
24. Liebisch, G., B. Lieser, J. Rathenberg, W. Drobnik, and G. Schmitz. 2004. High-throughput quantification of phosphatidylcholine and sphingomyelin by electrospray ionization tandem mass spectrometry coupled with isotope correction algorithm. *Biochim. Biophys. Acta.* **1686:** 108–117.
25. Valianpour, F., J. J. Selhorst, L. E. van Lint, A. H. van Gennip, R. J. Wanders, and S. Kemp. 2003. Analysis of very long-chain fatty acids using electrospray ionization mass spectrometry. *Mol. Genet. Metab.* **79:** 189–196.
26. Samanez, C. H., S. Caron, O. Briand, H. Dehondt, I. Duplan, F. Kuipers, N. Hennuyer, V. Clavey, and B. Staels. 2012. The human hepatocyte cell lines IHH and HepaRG: models to study glucose, lipid and lipoprotein metabolism. *Arch. Physiol. Biochem.* **118:** 102–111.
27. Ishii, M., A. Maeda, S. Tani, and M. Akagawa. 2015. Palmitate induces insulin resistance in human HepG2 hepatocytes by enhancing ubiquitination and proteasomal degradation of key insulin signaling molecules. *Arch. Biochem. Biophys.* **566:** 26–35.
28. Joshi-Barve, S., S. S. Barve, W. Butt, J. Klein, and C. J. McClain. 2003. Inhibition of proteasome function leads to NF-kappaB-independent IL-8 expression in human hepatocytes. *Hepatology.* **38:** 1178–1187.
29. Cansby, E., M. Amrutkar, L. Manneras Holm, A. Nerstedt, A. Reyahi, E. Stenfeldt, J. Boren, P. Carlsson, U. Smith, J. R. Zierath, et al. 2013. Increased expression of STK25 leads to impaired glucose utilization and insulin sensitivity in mice challenged with a high-fat diet. *FASEB J.* **27:** 3660–3671.
30. Tyanova, S., T. Temu, P. Sinitcyn, A. Carlson, M. Y. Hein, T. Geiger, M. Mann, and J. Cox. 2016. The Perseus computational platform for comprehensive analysis of (prote)omics data. *Nat. Methods.* **13:** 731–740.
31. Jägerström, S., S. Polesie, Y. Wickström, B. R. Johansson, H. D. Schröder, K. Højlund, and P. Boström. 2009. Lipid droplets interact with mitochondria using SNAP23. *Cell Biol. Int.* **33:** 934–940.
32. Wang, H., U. Sreenivasan, H. Hu, A. Saladino, B. M. Polster, L. M. Lund, D. W. Gong, W. C. Stanley, and C. Sztalryd. 2011. Perilipin 5, a lipid droplet-associated protein, provides physical and metabolic linkage to mitochondria. *J. Lipid Res.* **52:** 2159–2168. [Erratum. 2013. *J. Lipid Res.* 54: 3539.]
33. Su, W., Y. Wang, X. Jia, W. Wu, L. Li, X. Tian, S. Li, C. Wang, H. Xu, J. Cao, et al. 2014. Comparative proteomic study reveals 17beta-HSD13 as a pathogenic protein in nonalcoholic fatty liver disease. *Proc. Natl. Acad. Sci. USA.* **111:** 11437–11442.
34. Olsen, L. R., U. J. Kudahl, C. Simon, J. Sun, C. Schonbach, E. L. Reinherz, G. L. Zhang, and V. Brusic. 2013. BlockLogo: visualization of peptide and sequence motif conservation. *J. Immunol. Methods.* **400–401:** 37–44.
35. Matsuki, T., J. Chen, and B. W. Howell. 2013. Acute inactivation of the serine-threonine kinase Stk25 disrupts neuronal migration. *Neural Dev.* **8:** 21.
36. Lim, S., N. Hermance, T. Mudianto, H. M. Mustaly, I. P. M. Mauricio, M. A. Vittoria, R. J. Quinton, B. W. Howell, H. Cornils, A. L. Manning, et al. 2019. Identification of the kinase STK25 as an upstream activator of LATS signaling. *Nat. Commun.* **10:** 1547.
37. Voss, K., S. Stahl, B. M. Hogan, J. Reinders, E. Schleider, S. Schulte-Merker, and U. Felbor. 2009. Functional analyses of human and zebrafish 18-amino acid in-frame deletion pave the way for domain mapping of the cerebral cavernous malformation 3 protein. *Hum. Mutat.* **30:** 1003–1011.
38. Preisinger, C., B. Short, V. De Corte, E. Bruyneel, A. Haas, R. Kopajtich, J. Gettemans, and F. A. Barr. 2004. YSK1 is activated by the Golgi matrix protein GM130 and plays a role in cell migration through its substrate 14–3-3zeta. *J. Cell Biol.* **164:** 1009–1020.
39. Rakhshandehroo, M., B. Knoch, M. Muller, and S. Kersten. 2010. Peroxisome proliferator-activated receptor alpha target genes. *PPAR Res.* **2010:** 612089.
40. Toyama, T., H. Nakamura, Y. Harano, N. Yamauchi, A. Morita, T. Kirishima, M. Minami, Y. Itoh, and T. Okanoue. 2004. PPARalpha ligands activate antioxidant enzymes and suppress hepatic fibrosis in rats. *Biochem. Biophys. Res. Commun.* **324:** 697–704.
41. Ghosh, D., and J. M. Berg. 2010. A proteome-wide perspective on peroxisome targeting signal 1(PTS1)-Pex5p affinities. *J. Am. Chem. Soc.* **132:** 3973–3979.

42. Abdelraheim, S. R., D. G. Spiller, and A. G. McLennan. 2003. Mammalian NADH diphosphatases of the Nudix family: cloning and characterization of the human peroxisomal NUDT12 protein. *Biochem. J.* **374:** 329–335.
43. Hunt, M. C., M. I. Siponen, and S. E. Alexson. 2012. The emerging role of acyl-CoA thioesterases and acyltransferases in regulating peroxisomal lipid metabolism. *Biochim. Biophys. Acta.* **1822:** 1397–1410.
44. Williams, C. P., N. Schueller, C. A. Thompson, M. van den Berg, S. D. Van Haren, R. Erdmann, C. S. Bond, B. Distel, W. Schliebs, M. Wilmanns, et al. 2011. The peroxisomal targeting signal 1 in sterol carrier protein 2 is autonomous and essential for receptor recognition. *BMC Biochem.* **12:** 12.
45. Lodhi, I. J., and C. F. Semenkovich. 2014. Peroxisomes: a nexus for lipid metabolism and cellular signaling. *Cell Metab.* **19:** 380–392.
46. Baes, M., P. Gressens, E. Baumgart, P. Carmeliet, M. Casteels, M. Fransen, P. Evrard, D. Fahimi, P. E. Declercq, D. Collen, et al. 1997. A mouse model for Zellweger syndrome. *Nat. Genet.* **17:** 49–57.
47. Shimozawa, N., Z. Zhang, Y. Suzuki, A. Imamura, T. Tsukamoto, T. Osumi, Y. Fujiki, T. Orii, P. G. Barth, R. J. Wanders, et al. 1999. Functional heterogeneity of C-terminal peroxisome targeting signal 1 in PEX5-defective patients. *Biochem. Biophys. Res. Commun.* **262:** 504–508.
48. Senkal, C. E., M. F. Salama, A. J. Snider, J. J. Allopenna, N. A. Rana, A. Koller, Y. A. Hannun, and L. M. Obeid. 2017. Ceramide is metabolized to acylceramide and stored in lipid droplets. *Cell Metab.* **25:** 686–697.
49. Tanaka, S., H. Hikita, T. Tatsumi, R. Sakamori, Y. Nozaki, S. Sakane, Y. Shiode, T. Nakabori, Y. Saito, N. Hiramatsu, et al. 2016. Rubicon inhibits autophagy and accelerates hepatocyte apoptosis and lipid accumulation in nonalcoholic fatty liver disease in mice. *Hepatology.* **64:** 1994–2014.
50. Zhang, Y. L., H. Guo, C. S. Zhang, S. Y. Lin, Z. Yin, Y. Peng, H. Luo, Y. Shi, G. Lian, C. Zhang, et al. 2013. AMP as a low-energy charge signal autonomously initiates assembly of AXIN-AMPK-LKB1 complex for AMPK activation. *Cell Metab.* **18:** 546–555.
51. Ricchi, M., M. R. Odoardi, L. Carulli, C. Anzivino, S. Ballestri, A. Pinetti, L. I. Fantoni, F. Marra, M. Bertolotti, S. Banni, et al. 2009. Differential effect of oleic and palmitic acid on lipid accumulation and apoptosis in cultured hepatocytes. *J. Gastroenterol. Hepatol.* **24:** 830–840.
52. Quehenberger, O., A. M. Armando, A. H. Brown, S. B. Milne, D. S. Myers, A. H. Merrill, S. Bandyopadhyay, K. N. Jones, S. Kelly, R. L. Shaner, et al. 2010. Lipidomics reveals a remarkable diversity of lipids in human plasma. *J. Lipid Res.* **51:** 3299–3305.
53. Welte, M. A. 2007. Proteins under new management: lipid droplets deliver. *Trends Cell Biol.* **17:** 363–369.
54. Cipolla, C. M., and I. J. Lodhi. 2017. Peroxisomal dysfunction in age-related diseases. *Trends Endocrinol. Metab.* **28:** 297–308.
55. Kanda, T., S. Matsuoka, M. Yamazaki, T. Shibata, K. Nirei, H. Takahashi, T. Kaneko, M. Fujisawa, T. Higuchi, H. Nakamura, et al. 2018. Apoptosis and non-alcoholic fatty liver diseases. *World J. Gastroenterol.* **24:** 2661–2672.
56. Puri, P., F. Mirshahi, O. Cheung, R. Natarajan, J. W. Maher, J. M. Kellum, and A. J. Sanyal. 2008. Activation and dysregulation of the unfolded protein response in nonalcoholic fatty liver disease. *Gastroenterology.* **134:** 568–576.
57. Ibrahim, S. H., Y. Akazawa, S. C. Cazanave, S. F. Bronk, N. A. Elmi, N. W. Werneburg, D. D. Billadeau, and G. J. Gores. 2011. Glycogen synthase kinase-3 (GSK-3) inhibition attenuates hepatocyte lipoapoptosis. *J. Hepatol.* **54:** 765–772.
58. Cansby, E., N. M. Kulkarni, E. Magnusson, Y. Kurhe, M. Amrutkar, A. Nerstedt, M. Stahlman, C. Sihlbom, H. U. Marschall, J. Boren, et al. 2019. Protein kinase MST3 modulates lipid homeostasis in hepatocytes and correlates with nonalcoholic steatohepatitis in humans. *FASEB J.* **33:** 9974–9989.
59. Neuberger, G., S. Maurer-Stroh, B. Eisenhaber, A. Hartig, and F. Eisenhaber. 2003. Prediction of peroxisomal targeting signal 1 containing proteins from amino acid sequence. *J. Mol. Biol.* **328:** 581–592.
60. Neuberger, G., S. Maurer-Stroh, B. Eisenhaber, A. Hartig, and F. Eisenhaber. 2003. Motif refinement of the peroxisomal targeting signal 1 and evaluation of taxon-specific differences. *J. Mol. Biol.* **328:** 567–579.
61. Yifrach, E., S. Fischer, S. Oeljeklaus, M. Schuldiner, E. Zalckvar, and B. Warscheid. 2018. Defining the mammalian peroxisomal proteome. *Subcell. Biochem.* **89:** 47–66.
62. Schuster, S., D. Cabrera, M. Arrese, and A. E. Feldstein. 2018. Triggering and resolution of inflammation in NASH. *Nat. Rev. Gastroenterol. Hepatol.* **15:** 349–364.
63. Ipsen, D. H., J. Lykkesfeldt, and P. Tveden-Nyborg. 2018. Molecular mechanisms of hepatic lipid accumulation in non-alcoholic fatty liver disease. *Cell. Mol. Life Sci.* **75:** 3313–3327.
64. Wang, G., H. L. Bonkovsky, A. de Lemos, and F. J. Burczynski. 2015. Recent insights into the biological functions of liver fatty acid binding protein 1. *J. Lipid Res.* **56:** 2238–2247.
65. Gong, Y., G. Wang, Y. Gong, J. Yan, Y. Chen, and F. J. Burczynski. 2014. Hepatoprotective role of liver fatty acid binding protein in acetaminophen induced toxicity. *BMC Gastroenterol.* **14:** 44.
66. Picklo, M. J., E. K. Long, and E. E. Vomhof-DeKrey. 2015. Glutathionyl systems and metabolic dysfunction in obesity. *Nutr. Rev.* **73:** 858–868.
67. Yan, J., Y. Gong, Y. M. She, G. Wang, M. S. Roberts, and F. J. Burczynski. 2009. Molecular mechanism of recombinant liver fatty acid binding protein's antioxidant activity. *J. Lipid Res.* **50:** 2445–2454.
68. Wang, G., Y. Gong, J. Anderson, D. Sun, G. Minuk, M. S. Roberts, and F. J. Burczynski. 2005. Antioxidative function of L-FABP in L-FABP stably transfected Chang liver cells. *Hepatology.* **42:** 871–879.
69. Lu, L., A. K. Pandey, M. T. Houseal, and M. K. Mulligan. 2016. The genetic architecture of murine glutathione transferases. *PLoS One.* **11:** e0148230.
70. Atshaves, B. P., S. M. Storey, H. Huang, and F. Schroeder. 2004. Liver fatty acid binding protein expression enhances branched-chain fatty acid metabolism. *Mol. Cell. Biochem.* **259:** 115–129.
71. Atshaves, B. P., A. L. McIntosh, H. R. Payne, J. Mackie, A. B. Kier, and F. Schroeder. 2005. Effect of branched-chain fatty acid on lipid dynamics in mice lacking liver fatty acid binding protein gene. *Am. J. Physiol. Cell Physiol.* **288:** C543–C558.
72. Atshaves, B. P., A. M. McIntosh, O. I. Lyuksyutova, W. Zipfel, W. W. Webb, and F. Schroeder. 2004. Liver fatty acid-binding protein gene ablation inhibits branched-chain fatty acid metabolism in cultured primary hepatocytes. *J. Biol. Chem.* **279:** 30954–30965.
73. Antonenkov, V. D., R. T. Sormunen, S. Ohlmeier, L. Amery, M. Fransen, G. P. Mannaerts, and J. K. Hiltunen. 2006. Localization of a portion of the liver isoform of fatty-acid-binding protein (L-FABP) to peroxisomes. *Biochem. J.* **394:** 475–484.
74. Xu, W., L. Wu, M. Yu, F. J. Chen, M. Arshad, X. Xia, H. Ren, J. Yu, L. Xu, D. Xu, et al. 2016. Differential roles of cell death-inducing DNA fragmentation factor-alpha-like effector (CIDE) proteins in promoting lipid droplet fusion and growth in subpopulations of hepatocytes. *J. Biol. Chem.* **291:** 4282–4293.
75. Zhou, L., L. Xu, J. Ye, D. Li, W. Wang, X. Li, L. Wu, H. Wang, F. Guan, and P. Li. 2012. Cidea promotes hepatic steatosis by sensing dietary fatty acids. *Hepatology.* **56:** 95–107.
76. Zhou, Z., S. Yon Toh, Z. Chen, K. Guo, C. P. Ng, S. Ponniah, S. C. Lin, W. Hong, and P. Li. 2003. Cidea-deficient mice have lean phenotype and are resistant to obesity. *Nat. Genet.* **35:** 49–56.
77. Hornbeck, P. V., B. Zhang, B. Murray, J. M. Kornhauser, V. Latham, and E. Skrzypek. 2015. PhosphoSitePlus, 2014: mutations, PTMs and recalibrations. *Nucleic Acids Res.* **43:** D512–D520.
78. Dobrikov, M. I., E. Y. Dobrikova, and M. Gromeier. 2013. Dynamic regulation of the translation initiation helicase complex by mitogenic signal transduction to eukaryotic translation initiation factor 4G. *Mol. Cell. Biol.* **33:** 937–946.
79. Sudhir, P. R., C. L. Hsu, M. J. Wang, Y. T. Wang, Y. J. Chen, T. Y. Sung, W. L. Hsu, U. C. Yang, and J. Y. Chen. 2011. Phosphoproteomics identifies oncogenic Ras signaling targets and their involvement in lung adenocarcinomas. *PLoS One.* **6:** e20199.
80. Perez-Riverol, Y., A. Csordas, J. W. Bai, M. Bernal-Llinares, S. Hewapathirana, D. J. Kundu, A. Inuganti, J. Griss, G. Mayer, M. Eisenacher, et al. 2019. The PRIDE database and related tools and resources in 2019: improving support for quantification data. *Nucleic Acids Res.* **47:** D442–D450.